

# 3D MRA Coronary Axis Determination Using a Minimum Cost Path Approach

Onno Wink,<sup>1\*</sup> Alejandro F. Frangi,<sup>1</sup> Bert Verdonck,<sup>2</sup> Max A. Viergever,<sup>1</sup> and Wiro J. Niessen<sup>1</sup>

**A method is introduced to automatically find the coronary axis based on two or more user-defined points, even in the presence of a severe stenosis. The coronary axis is determined by finding a minimum cost path (MCP) in a feature image in which the tubular-like structures are enhanced. The results of the proposed method were compared with manually drawn central axes to estimate the accuracy. In 32 3D TFE-EPI acquisitions of patients and volunteers, 14 right coronary arteries (RCAs), 15 left anterior descending arteries (LADs), and eight left circumflex arteries (LCXs) were manually tracked twice by two operators to determine a reference axis and to assess the inter- and intra-user variability. On average, the maximum distance to the reference axis, based on only two user-defined points, is less than 1.5 mm; the average distance is around 0.65 mm, which is less than the average in-plane resolution. The results of the method are comparable to those of the manual operators. Magn Reson Med 47:1169–1175, 2002. © 2002 Wiley-Liss, Inc.**

**Key words:** 3D coronary MRA; central vessel axis; vessel visualization; minimum cost path; quantitative coronary analysis

In the last few years several magnetic resonance angiography (MRA) acquisition methods have been introduced which provide 3D images of the coronary arteries with good signal-to-noise (SNR) and contrast-to-noise (CNR) ratios (1–6). However, because of the tortuous nature of the coronaries, it is not possible to capture a long stretch of vessel in a single plane. Postprocessing is therefore required to obtain a proper visualization of the coronaries in 3D space. Although a large variety of approaches have been proposed to facilitate the diagnosis of vessel segments (e.g., 7–15), relatively few have addressed the problems that occur in the case of a (severe) stenosis or in the presence of image artifacts, in which case there is hardly any image evidence to guide the algorithm. Especially iterative tracking and region-growing procedures experience difficulties in these cases (see Fig. 1a).

Determining a minimum cost path (MCP) (e.g., 16–23) between two or more user-defined points is an alternative way to handle these situations (see Fig. 1b).

In this article it is investigated whether the latter approach, in combination with a filter that enhances tubular-like structures, is suitable for tracking the coronary arteries

automatically between two or more user-defined points. The result of the MCP approach is an estimate of the central coronary axis, which can serve as input for a subsequent visualization and quantification procedure. The method is applied to a number of 3D MRA images, and the results are compared with those of two human operators to determine the accuracy and applicability of the method.

## METHODS

### Image Acquisition

The images are acquired on a 1.5 Tesla Philips Gyroscan ACS-NT MR scanner, using a navigator gated and corrected ECG triggered ultra-fast 3D interleaved gradient turbo field echo-echo planar imaging (TFE-EPI) sequence, preceded by fat- and muscle-suppressing pulses. For a detailed description of the imaging sequence, see Botnar et al. (6). The images consist of 20 slices of  $512 \times 512$  pixels, and a reconstructed slice thickness of 1.5 mm. The field of view (FOV) is either 360 or 370 mm. A total of 32 images are acquired from both patients (29%) and volunteers (71%). A three-point plan scan is used to align the center plane in the final acquisition with the coronary artery of interest.

### Image Processing

Figure 2 shows the different phases of our technique in a slice of the original 3D dataset, containing the right coronary artery (RCA). To illustrate the strength of the approach, two stenoses are created artificially (Fig. 2a). First, tubular structures are enhanced in the image using a special-purpose multiscale eigenvalue filter (Fig. 2b). The output of this filter is used in an MCP approach to determine the coronary axis between two user-defined points (Fig. 2c and d).

### Vessel Enhancement

First, the original data is filtered with a special-purpose multiscale filter based on eigenvalue analysis of the Hessian matrix (24–26). This filter is designed to highlight tubular structures in the image and is capable of coping with anisotropic voxels and vessels with varying width. The idea behind the eigenvalue analysis of the Hessian is to extract the principal directions in which the local second-order structure of the image can be decomposed. Since this directly gives the direction of smallest curvature (along the vessel), the application of several filters in multiple orientations is avoided. The latter approach is computationally more expensive and requires a discretization

<sup>1</sup>Image Sciences Institute, University Medical Center, Utrecht, The Netherlands.

<sup>2</sup>EasyVision Advanced Development, Philips Medical Systems BV, Best, The Netherlands.

Grant sponsor: EasyVision Advanced Development, Philips Medical Systems BV.

\*Correspondence to: Onno Wink, UMC Utrecht, Room E01.334, Heidelberglaan 100, 3584 CX Utrecht, The Netherlands. E-mail: onno@isi.uu.nl

Received 10 July 2001; revised 1 February 2002; accepted 1 February 2002.

DOI 10.1002/mrm.10164

Published online in Wiley InterScience (www.interscience.wiley.com).

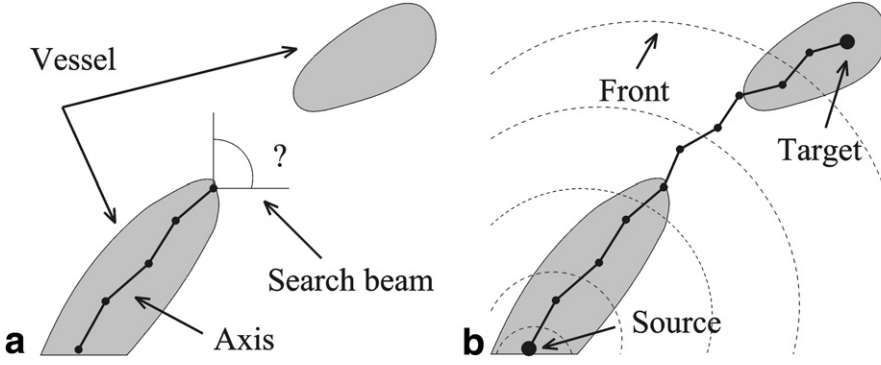


FIG. 1. **a:** Situation in which an iterative line tracker, based on local information, does not know how to proceed in the case of a severe stenosis or imaging artifact. **b:** The use of wave propagation to find an MCP between a source node and a target node does achieve an estimate of the vessel axis.

of the orientation space. The Hessian matrix  $H_{\sigma}$  at a given voxel is defined as:

$$H_{\sigma} = \begin{bmatrix} L_{xx} & L_{xy} & L_{xz} \\ L_{yx} & L_{yy} & L_{yz} \\ L_{zx} & L_{zy} & L_{zz} \end{bmatrix} \quad [1]$$

where  $\sigma$  denotes the scale of the Gaussian kernel used for regularizing the derivative operator involved in the computation of the normalized second-order Gaussian derivatives (27) of the original image  $I(\mathbf{x})$ :

$$L_{uv}(\mathbf{x}, \sigma) = \sigma^2 \frac{\partial^2 G(\mathbf{x}, \sigma)}{\partial u \partial v} * I(\mathbf{x}) \quad G(\mathbf{x}, \sigma) = \frac{1}{\sqrt{(2\pi\sigma^2)^3}} e^{-\|\mathbf{x}\|^2/2\sigma^2}. \quad [2]$$

The second-order derivative can be represented as a probe kernel that measures the contrast between the regions inside and outside the range  $(-\sigma, \sigma)$  in the direction of the derivative (Fig. 3a).

The anisotropy of the dataset is handled by adjusting the parameter vector  $\sigma$  in each direction. For an ideal tubular structure, the eigenvalues, when sorted in increasing magnitude, will obey the following rules:

$$|\lambda_1| \approx 0 \quad [3]$$

$$|\lambda_1| \ll |\lambda_2| \quad [4]$$

$$\lambda_2 \approx \lambda_3. \quad [5]$$

The corresponding eigenvectors are given in Fig. 3b. The eigenvector in the direction of the vessel corresponds to the smallest eigenvalue  $\lambda_1$ , while the eigenvectors that correspond to the larger eigenvalues  $\lambda_2$  and  $\lambda_3$  span a plane orthogonal to the vessel. Based on these observations, Lorenz et al. (26) proposed a filter  $R(\sigma)$ :

$$R(\sigma) = \begin{cases} 0 & \text{if } \lambda_2 > 0 \text{ or } \lambda_3 > 0 \\ |\lambda_2 + \lambda_3| & \text{otherwise} \end{cases}. \quad [6]$$

The response of the filter is expected to be maximum at a scale that approximates the radius of the coronary. The response at different scales can be combined by taking the maximum response over a range of scales.

#### Minimum Cost Path

Based on two (or more) user-defined points in the coronary of interest, an estimate of the central coronary axis is determined using an MCP search (Fig. 2c and d). In the MCP approach, as originally proposed by Dijkstra (28), the image is treated as a grid of nodes, where every node/voxel is connected to a number of neighbors, e.g., a six- or 26-node neighborhood. The transition cost of traveling from node  $n$  to its neighbor  $n'$  is given by the arc costs  $a(n, n')$ , which corresponds to the reciprocal output of the filter ( $R$ , see Eq. [6]) at the neighboring node  $n'$ . Based on the source node  $s$ , a search process is initiated to find all subpaths of minimum costs, which will continue until the goal node  $g$  is found. This search process can be regarded as the propagation of a wave front, initiated from a source

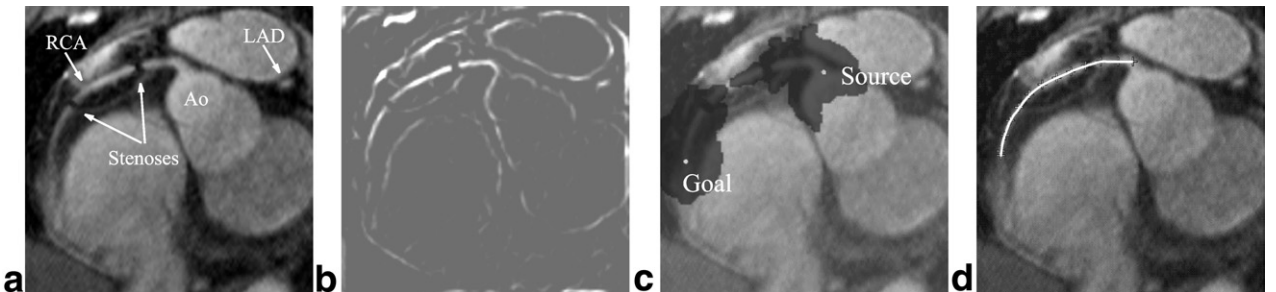
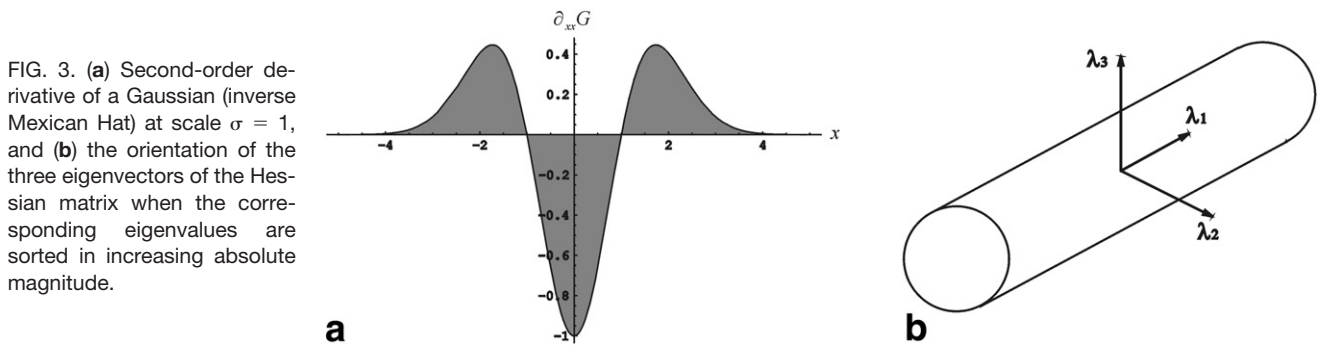


FIG. 2. **a:** Part of a slice from a 3D MRA dataset containing the RCA and two artificially created stenoses. **b:** The response of a 2D eigenvalue filter. **c:** The pixels that are visited during a 2D bidirectional MCP search that is started in two user-defined points. **d:** The (resampled) MCP found.



$s$ , over the voxels in the image. The intensities of the voxels influence the velocity of the propagating wave. The process ends if the wave front reaches the goal node  $g$ . The path to the source node  $s$  can subsequently be retrieved by tracing back the predecessors of the node that corresponds to the goal node  $g$ . The approach is implemented via a traditional MCP algorithm, wherein a priority queue (29) is used to maintain the list of temporary nodes  $t$ , holding the nodes that make up the wave front. For a detailed discussion about obtaining MCPs with subpixel accuracy, see Sethian (23).

Figure 2c displays an example of a stage in the MCP approach. The pixels that are visited during the search process are highlighted. In this example, a search process is started in the source node  $s$  as well as in the goal node  $g$  in order to speed up the computation time without violating the result of the MCP (20). This bidirectional search process is terminated when the two wave fronts meet. The result is an MCP between the nodes  $s$  and  $g$ , as shown in Fig. 2d.

If the gap between two portions of a vessel is too large, the MCP may choose to find an alternative route, such as the border of the cardiac chamber or other enhanced structures, as displayed in Fig. 2b. However, the cost of skipping to another vessel-like structure requires two transitions and, often, a long route. It can therefore only occur if the other vessel is enhanced to the same extent as the vessel of interest, and is situated next to the vessel of interest. Moreover, the other vessel should be located near the vessel of interest both before and after the stenotic region. Otherwise, the cost of the path back to the goal node will be too high, since it is very likely to pass through non-enhanced structures in order to still arrive at this goal

node. In practice, the stenotic region is generally neither too large nor entirely blocked. The chance for an alternative route depends on the discriminative power of the filter and on the difference in path length. In the following section, the MCP in combination with the previously-described vessel-enhancing filter (Eq. [6]) is applied to determine the vessel axis of different lengths of the main coronary vessels. Once the MCP is found, it can be used for subsequent visualizations, as shown in Fig. 4, or as input for additional quantification procedures (e.g., 9,30–32).

#### Implementation Details

The cost images used in the MCP search are computed using a multiscale filter as proposed by Lorenz et al. (26) (Eq. [6]). The filter is applied both at a range of scales ( $\sigma_x = 0.5$  mm to  $\sigma_x = 1.5$  mm, with linear steps of 0.1 mm), and at a single scale, corresponding to an estimate of the average radius of the coronary at hand, i.e., 1.0 mm for the LAD and RCA, and 0.8 mm for the LCX. To speed up the computation time, and to better cope with the relative small vessel diameters, the actual convolution is performed using a multiplication in Fourier space. Furthermore, the Gaussian second-order derivatives at the different scales are precomputed in Fourier space. A bidirectional search and a 26-node neighborhood is used in the determination of the MCP.

#### Evaluation

To assess the performance of the method, the resulting MCPs are compared with tracings of human operators. First, the difference between the automated method and

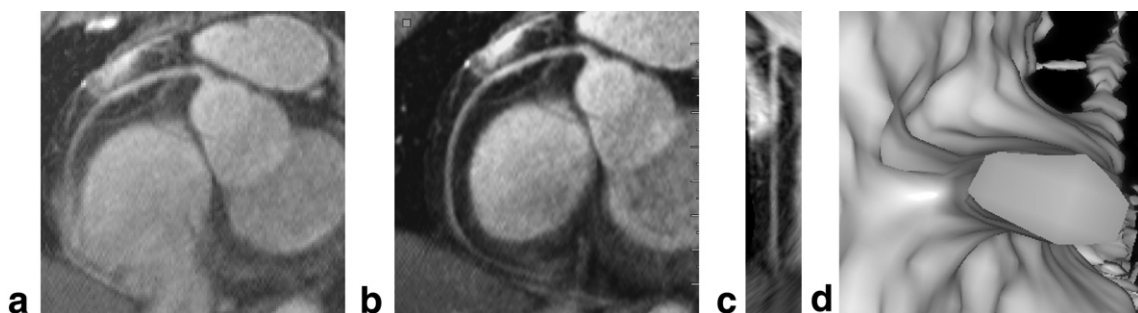


FIG. 4. Examples of central axis-based visualizations based on (a) the original image, i.e., (b) curved reformat clearly displaying a larger portion of the RCA by using the information from several slices, (c) straightened reformat, and (d) virtual fly-through.

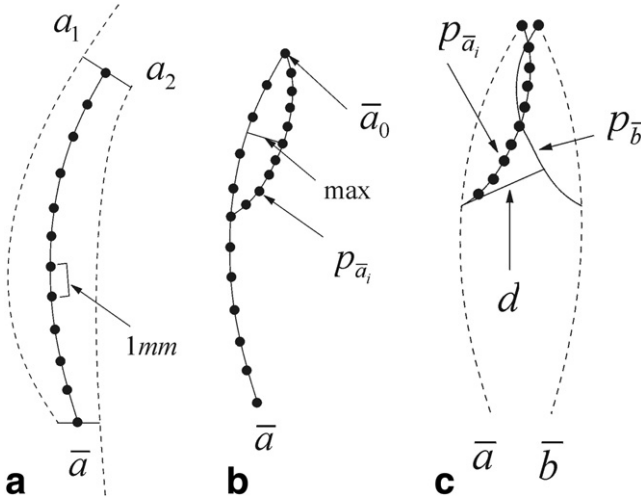


FIG. 5. **a:** The construction of an average path  $\bar{a}$  based on the trajectories of two manually determined paths  $a_1$  and  $a_2$ . The differences between the average path and the individual paths determine the intra-operator difference. **b:** Example of comparing the MCP  $p_{\bar{a}_n}$  to the average path  $\bar{a}$ . The MCP is found based on the first point  $\bar{a}_0$  and the fifth sample point 5 mm away from the first point of the average path  $\bar{a}$ . The nodes  $p_{\bar{a}_n}(i)$  that make up this MCP are traversed to find the maximum and average distance to the very densely resampled version of the average path  $\bar{a}$ . **c:** Example of comparing two MCPs based on different begin- and end-points, used to determine the robustness of the method to user initialization.

the individual operators is quantified and compared to the differences between the operators to determine whether the automated method can replace manual operators. Second, the robustness of the method is tested by varying the user-initialized points. Intra-operator variability can be assessed since all manual tracings were performed twice. Because it may be expected that performance of both manual operators and the automated method depend on the length of the tracked coronary axis, all evaluations are carried out with multiple segment lengths. Although the MCP search can be used to find a path through an arbitrary number of user-initialized points on the vessel segment, only the begin- and end-points of the segment are used in the evaluation.

For every dataset the central coronary axis is manually determined starting from the trunk of the ascending aorta (Ao). A total of 14 RCA, 15 LAD, and eight LCX were manually tracked on a Philips EasyVision workstation running version R4.2.2.2. This procedure was repeated after two weeks. As a result, four manually drawn paths ( $a_1$ ,  $a_2$ ,  $b_1$ ,  $b_2$ ) are acquired for every coronary in the datasets. The two axes of every operator are averaged by first determining their corresponding part and subsequently sampling these paths in an equal number of points (Fig. 5a).

The origins of the resulting axes  $\bar{a}$  and  $\bar{b}$  serve as starting points for the MCP process, while the end-points are obtained by resampling the average axes  $\bar{a}$  and  $\bar{b}$  every millimeter. Thus MCPs are obtained for varying segment lengths, which are denoted by  $p_{\bar{a}_n}$  and  $p_{\bar{b}_n}$ , respectively, where the subscript  $n$  denotes the end-point number. For

every cost path  $p_{\bar{a}_n}$  and  $p_{\bar{b}_n}$ , the average and maximum distances to the operator paths are computed (Fig. 5b and c):

$$dist_{\max} = \frac{\max(d(p_{\bar{a}_n}(i), \bar{a})) + \max(d(p_{\bar{b}_n}(i), \bar{b}))}{2}, \quad 0 \leq i \leq N \quad [7]$$

$$dist_{\text{average}} = \sum_{i=0}^N \frac{d(p_{\bar{a}_n}(i), \bar{a}) + d(p_{\bar{b}_n}(i), \bar{b})}{2N} \quad [8]$$

where  $d(p_{\bar{a}_n}(i), \bar{a})$  denotes the minimum distance between the  $i$ -th node of the MCP  $p_{\bar{a}_n}$  and a very densely resampled average path  $\bar{a}$  (see Fig. 5b), and  $N$  is the total number of nodes in the MCP.

To determine inter-operator variation, the individual axes of one operator are compared with the average axis of the other ( $\bar{a}$  and  $\bar{b}$ , respectively, in Eqs. [7] and [8]):

$$inter_{\max} = \frac{\max(d(a_1(i), \bar{b})) + \max(d(a_2(i), \bar{b})) + \max(d(b_1(i), \bar{a})) + \max(d(b_2(i), \bar{a}))}{4}, \quad 0 \leq i \leq N \quad [9]$$

$inter_{\text{average}}$

$$= \sum_{i=0}^N \frac{d(a_1(i), \bar{b}) + d(a_2(i), \bar{b}) + d(b_1(i), \bar{a}) + d(b_2(i), \bar{a})}{4N}. \quad [10]$$

Here  $N$  is the total number of nodes in the reference axis, while  $d(a_1(i), \bar{b})$  denotes the minimum distance between the  $i$ -th sample point of the axis  $a_1$  located at a distance of  $i$  mm from its origin, and a very densely resampled average path  $\bar{b}$ .

To determine the robustness of the automated method with respect to the variation in the positioning of the begin- and end-points, MCPs based on  $\bar{a}$  and  $\bar{b}$  are compared:

$$mcp_{\text{average}} = \sum_{i=0}^N \frac{d(p_{\bar{a}_n}(i), p_{\bar{b}_n}) + d(p_{\bar{b}_n}(i), p_{\bar{a}_n})}{2N}. \quad [11]$$

Here  $d(p_{\bar{a}_n}(i), p_{\bar{b}_n})$  denotes the minimum distance of the  $i$ -th point in the MCP  $p_{\bar{a}_n}$ , based on the begin- and end-points of the average path  $\bar{a}$ , to a very densely resampled version of the corresponding MCP  $p_{\bar{b}_n}$ , based on the average path  $\bar{b}$  (see Fig. 5c).

The average differences within the individual operators (intra-operator) is computed as follows:

$$intra_{\max} = \frac{\max(d(\bar{a}(i), a_1)) + \max(d(\bar{a}(i), a_2)) + \max(d(\bar{b}(i), b_1)) + \max(d(\bar{b}(i), b_2))}{4}, \quad 0 \leq i \leq N \quad [12]$$



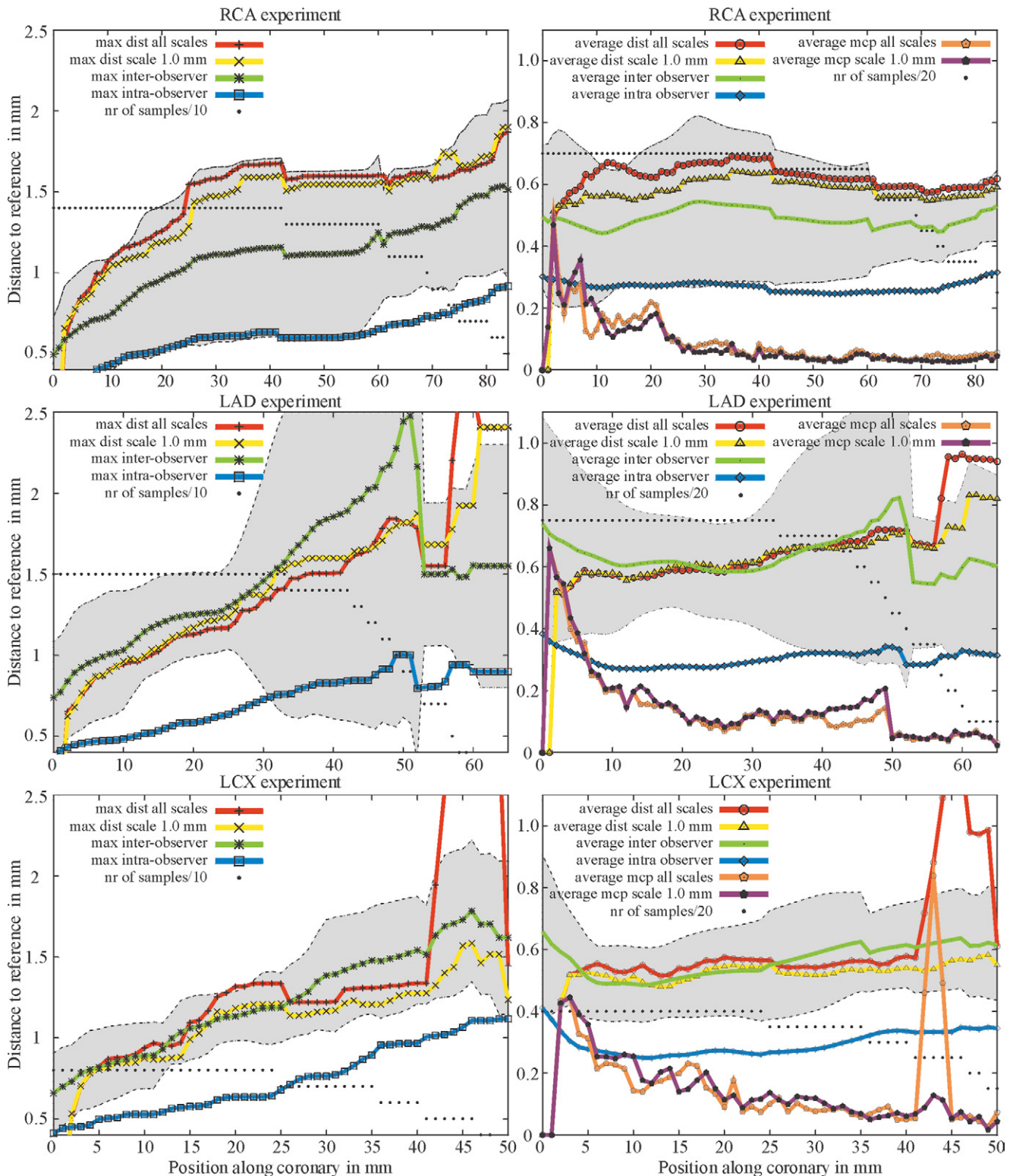


FIG. 6. The results of the evaluation over all the datasets for the three coronary axes: RCA (top row), LAD (middle row) and LCX (bottom row). The results are presented in two columns. The maximum measures are given in the left column, and the average measures are given in the right. For the automated method, both the results based on the response of a filter using a range of scales (red lines) and at a single scale (yellow lines) are shown. These should be compared to the inter-observer performance (green line) and variation (gray shaded zone indicating region  $\pm\sigma$ ). It can be observed that the performance of the method is similar to that of the observers, except for the RCA. The reproducibility of the method is also tested (brown: all scales; purple: one scale) by selecting different initialization points. In all experiments the intra-method variability is consistently lower than the intra-observer variability (blue line). The number of coronary arteries used in the analysis is given as a reference (black dots).

$intra_{average}$

$$= \sum_{i=0}^N \frac{d(\bar{a}(i), a_1) + d(\bar{a}(i), a_2) + d(\bar{b}(i), b_1) + d(\bar{b}(i), b_2)}{4N}. \quad [13]$$

Where  $d(\bar{a}(i), a_1)$  denotes the minimum distance between the  $i$ -th sample point of the average axis  $\bar{a}$ , located at a distance of  $i$  mm from its origin and a very densely re-sampled average path  $a_1$ .

## RESULTS

The results of the comparison of the automated approach vs. the manual tracings are shown in Fig. 6.

The results are averaged over all the datasets for the RCA (upper row), LAD (middle row), and LCX (bottom row). All difference measures are given in millimeters. Since not all coronary arteries are of equal length, the number of coronaries included in the evaluation decreases with longer segments; the number of coronary arteries used in the analysis is given by the black dots as a reference. It is shown that for the automated methods the maximum distance to the observer's axes is less than 1.5 mm, while the average distance is around 0.65 mm, which is less than the average in-plane resolution of 0.71 mm. It can be observed that the performance based on the filter response at a single scale is almost equivalent to the performance based on the filter using a range of scales, with the exception of the LCX after about 41 mm, for which the single-scale filter performs better.

For the RCA, which is generally less tortuous than the other coronaries, the difference between the two observers is consistently smaller than the difference between the automated method and the observers. This holds for both the maximum distance and the average distance measures. For the LAD and LCX, however, the inter-observer distance is of the same order as the performance of the automated methods.

Although different types of measures are used, it is clear that the average differences between two MCPs ( $mcp_{average}$ ), based on small changes of the user-provided begin- and end-points, are significantly smaller than the average differences between the users.

The average computation time needed to determine a central axis estimate at a single scale is about 6 s on a 440 MHz Sun UltraSPARC with 1 gigabyte of RAM. The fast majority of the computation time is devoted to the enhancement of the vessels, which can be precomputed in a practical situation. The computation of the bidirectional MCP itself is performed almost instantaneously.

## DISCUSSION AND CONCLUSIONS

A method that combines a vessel enhancement filter and a minimum cost path approach to determine the vessel axis in the coronaries based on two user-defined points has been presented and evaluated. Whereas the special-purpose filter allows the use of multiple scales to capture vessels of varying width, it is shown that for a properly

selected single scale, i.e., corresponding to the expected radius of the coronary artery of interest, performance of the method is not degraded. For the LCX after about 41 mm, the single-scale filter performed even better. This effect can be explained by the fact that at the larger distances, the posterior vein of the left ventricle runs almost parallel to the LCX. In some of the acquisitions, this larger vein is very bright, while the contrast in the LCX is low, resulting in a higher filter output at a higher scale. As a result, the MCP is likely to follow this vein for a while before it continues through the actual LCX. From these findings it may be concluded that to speed up the vessel enhancement filtering a single scale may be used for the coronaries, provided that the proper scale is selected.

A comparison of results from the method with those of operators shows that the difference between observers is similar to the difference between the method and the observers for the LAD and LCX. The method performed slightly worse for the RCA. However, as expected, the automated method is more robust, as variations induced by small changes in the positioning of the begin- and end-points is considerably smaller than intra-operator variability.

A drawback of the traditional MCP approach is that the resulting path is obtained by making discrete steps from one voxel to the other. A smoother representation of the vessel axis can be obtained by reconstructing the original dataset or the filtered version at a higher resolution. Another alternative is to obtain a subpixel accurate path through a gradient descent from the goal node back to its source node using the cumulative costs in the nodes (23). These modifications may further improve the approach.

Due to the limited number of patients in this study, the evaluation of the method is biased towards the nonseverely stenosed coronaries. However, in practice, the lesion is generally neither too large nor entirely blocked. The proposed method has the potential to find an estimate of the central vessel axis, even in the case of a severe stenosis, although it may choose an alternative route if the gap is too large and another vessel-like structure is nearby.

Once a path is found, it can provide direct visualization of the coronary arteries over a long stretch of vessel. Furthermore, it can be used as a preprocessing step in the quantitative analysis of vessel morphology. Although the evaluation presented in this work is based on images that were acquired using the same scanning protocol, the applicability of the proposed method is not limited to these images. The method has the potential to be applied to different types of acquisitions, such as black-blood scans and regular contrast-enhanced MRA of the coronaries, and other vascular structures. Consequently, a feature extraction based on eigenvalue analysis, followed by an MCP approach to determine the central vessel axis, offers great potential for the visualization and analysis of vessels in 2D and 3D images.

## ACKNOWLEDGMENTS

We gratefully acknowledge Dr. W.J. Manning, Cardiac MR Center, Beth Israel Deaconess Medical Center, Boston, Massachusetts, for allowing the use of image data. F.A.

Gerritsen from Philips Medical Systems, Best, The Netherlands, is acknowledged for funding this research project.

## REFERENCES

1. van Geuns RJM, Wielopolski PA, de Bruin HG, Rensing BJWM, Hulshoff M, van Ooijen PMA, de Feyter PJ, Oudkerk M. MR coronary angiography with breath-hold targeted volumes: preliminary clinical results. *Radiology* 2000;217:270–277.
2. Fayad ZA, Fuster V, Fallon JT, Jayasundera T, Worthley SG, Helft G, Aguinaldo JG, Badimon JJ, Sharma SK. Noninvasive in vivo human coronary artery lumen and wall imaging using black blood magnetic resonance imaging. *Circulation* 2000;102:506–510.
3. Lorenz CH, Johansson LOM. Contrast-enhanced coronary MRA. *J Magn Reson Imaging* 1999;10:703–708.
4. Botnar RM, Stuber M, Danias PG, McConnel MV, Kissinger KV, Yucel EK, Manning WJ. Contrast agent-enhanced, free breathing three-dimensional coronary magnetic resonance angiography. *J Magn Reson Imaging* 1999;10:790–799.
5. Botnar RM, Stuber M, Danias PG, Kissinger KV, Manning WJ. Improved coronary artery definition with T2-weighted, free-breathing, three-dimensional coronary MRA. *Circulation* 1999;99:3139–3148.
6. Botnar RM, Stuber M, Danias PG, Kissinger KV, Manning WJ. A fast 3D approach for coronary MRA. *J Magn Reson Imaging* 1999;10:821–825.
7. Cline HE, Thedens DR, Meyer CH, Nishimura DG, Foo TK, Ludke S. Combined connectivity and a gray-level morphological filter in magnetic resonance coronary angiography. *Magn Reson Med* 2000;43:892–895.
8. Wink O, Niessen WJ, Viergever MA. Fast delineation and visualization of vessels in 3D angiographic images. *IEEE Trans Med Imaging* 2000; 9:337–436.
9. Hernández-Hoyos M, Anwender A, Orkisz M, Roux J-P, Douek P, Maguin IE. A deformable vessel model with single point initialization for segmentation, quantification and visualization of blood vessels in 3D MRA. In: *Proceedings of Medical Image Computing and Computer-Assisted Intervention*. Berlin: Springer-Verlag; 2000. p 735–745.
10. Cline HE, Thedens DR, Irarrazaval P, Meyer CH, Hu BS, Nishimura DG, Ludke S. 3D MR coronary artery segmentation. *Magn Reson Med* 1998; 40:697–702.
11. Noordmans HJ, Smeulders AWM. High accuracy tracking of 2D/3D curved line-structures by consecutive cross-section matching. *Pattern Recogn Lett* 1998;19:97–111.
12. Intensity ridge and widths for tubular object segmentation and description. In: Amini AA, Bookstein FL, editors. *Proceedings of the Workshop on Mathematical Methods in Biomedical Image Analysis*, 1996. p 131–138.
13. Ma CM, Sonka M. A fully 3D thinning algorithm and its applications. *Comput Vision Image Underst* 1996;64:420–433.
14. Klose U, Petersen D, Martos J. Tracking of cerebral vessels in MR angiography after highpass filtering. *Magn Reson Imaging* 1995;13:45–51.
15. Gerig G, Koller ThM, Székely G, Brechbühler Ch, Kübler O. Symbolic description of 3-D structures applied to cerebral vessel tree obtained from MR angiography volume data. In: Barrett HH, Gmitro AF, editors. *Proceedings of IPMI*. Berlin: Springer Verlag; 1993. p 94–111.
16. Deschamps T, Cohen LD. Fast extraction of minimal paths in 3D images and applications to virtual endoscopy. *Med Image Anal* 2001;5:281–299.
17. Quek FKH, Kirbas C. Vessel extraction in medical images by wave propagation and traceback. *IEEE Trans Med Imaging* 2001;20:117–131.
18. Law TY, Heng PA. Automatic centerline extraction for 3D virtual bronchoscopy. In: *Proceedings of Medical Image Computing and Computer-Assisted Intervention*. Berlin: Springer Verlag; 2000. p 786–795.
19. Avants BB, Williams JP. An adaptive minimal path generation technique for vessel tracking in CTA/CE-MRA volume image. In: *Proc. Proceedings of Medical Image Computing and Computer-Assisted Intervention*. Berlin: Springer Verlag; 2000. p 707–715.
20. Wink O, Niessen WJ, Viergever MA. Minimum cost path determination using a simple heuristic function. In: Sanfeliu A, Villanueva JJ, Vanrell J, Alquézar R, Huang T, Serra J, editors. In: *Proceedings of the 15th International Conference on Pattern Recognition, IEEE Computer Society*, 2000. p 1010–1013.
21. Falcao AX, Udupa JK, Miyazawa FK. An ultra-fast user-steered image segmentation paradigm: live wire on the fly. *IEEE Trans Med Imaging* 2000;19:946–956.
22. Deschamps T, Létang JM, Verdonck B, Cohen LD. Automatic construction of minimal paths in 3D images: an application to virtual endoscopy. In: *Proceedings of Computer Assisted Radiology and Surgery*, Amsterdam. Elsevier Publishers; 1999. p 151–155.
23. Sethian JA. *Level set methods and fast marching methods*, 2nd ed. Cambridge: Cambridge University Press; 1999.
24. Frangi AF, Niessen WJ, Vincken KL, Viergever MA. Vessel enhancement filtering. In: *Proceedings of Medical Image Computing and Computer-Assisted Intervention*. Berlin: Springer-Verlag; 1998. p 130–137.
25. Sato Y, Nakajima S, Shiraga N, Atsumi H, Yoshida S, Koller T, Gerig G, Kikinis R. Three-dimensional multi-scale line filter for segmentation and visualization of curvilinear structures in medical images. *Med Image Anal* 1998;2:143–168.
26. Lorenz C, Carlsen IC, Buzug TM, Fassnacht C, Weese J. Multi-scale line segmentation with automatic estimation of width, contrast and tangential direction in 2D and 3D medical images. In: *Proceedings of CVRMed and MRCAS*. Berlin: Springer Verlag; 1997. p 233–242.
27. Lindeberg T. Feature detection with automatic scale selection. *Int J Comput Vision* 1998;30:79–116.
28. Dijkstra E. A note on two problems in connexion with graphs. *Numerische Math* 1959;1:269–271.
29. Cherkassky BV, Goldberg AV, Silverstein C. Buckets, heaps, lists, and monotone priority queues. *SIAM J Comput* 1999;4:1326–1346.
30. Frangi AF, Niessen WJ, Hoogeveen RM, van Walsum TH, Viergever MA. Model-based quantitation of 3D magnetic resonance angiographic images. *IEEE Trans Med Imaging* 1999;18:946–956.
31. Westenberg JJM, van der Geest RJ, Wasser MNJM, Doornbos J, Patynama PMT, de Roos A, Vanderschoot J, Reiber JHC. Objective stenosis quantification from post-stenotic signal loss in phase-contrast magnetic resonance angiographic datasets of flow phantoms and renal arteries. *Magn Reson Imaging* 1998;16:249–260.
32. Verdonck B, Bloch I, Maître H, Vandermeulen D, Suetens P, Marchal G. Accurate segmentation of blood vessels from 3D medical images. In: *Proceedings of IEEE International Conference on Image Processing*, 1996. p 311–314.